Artificial Intelligence Technologies and Applications
C. Chen (Ed.)

© 2024 The Authors.
This article is published online with Open Access by IOS Press and distributed under the terms of the Creative Commons Attribution Non-Commercial License 4.0 (CC BY-NC 4.0).
doi:10.3233/FAIA231357

2D Numerical Aerodynamic Simulation for the Interpretation of Formation Flight Phenomena in Birds

Shengyou DUAN[1]
Leicester International Institute, Dalian University of Technology, Panjin, Liaoning Province, 124221, China

Abstract. Formation flight of birds is a common phenomenon in nature. Birds can fly efficiently in formation through close coordination and communication. With the rapid development of unmanned aerial vehicle (UAV) technology, formation flight has become one of the popular research topics. The study of the aerodynamic principle of bird formation flight can provide new ideas and methods for UAV formation flight. In this study, the household incompressible unsteady Navier-Stokes solver based on the finite volume method was used to study the aerodynamic characteristics of formation flight arranged in a straight line with second-order spatial and temporal discretization schemes. By numerical simulation of the flow field around two NACA0012 airfoils, the velocity, pressure gradient, and vorticity distribution around two airfoils in a two-dimensional (2D) plane were studied and the mechanical characteristics were analyzed. The following conclusions are drawn. In the linear formation flight, the rear airfoil has a higher lift coefficient, lower pressure drag coefficient, and lower viscous drag coefficient than the front one. Combined with the dynamic simulation, the principle of vortex shedding and wake interference as the cause of lift is explained from the perspective of vorticity.

Keywords: formation flight, wake interference, vorticity distribution, unsteadiness, 2D numerical simulation.

1. Introduction

The history of aircraft development can be traced back to ancient times when humans aspired to achieve avian flight. It was not until the late 19th and early 20th centuries that humans began to truly attempt to manufacture machines capable of carrying humans for flight. The Wright brothers were the first to successfully build an aircraft and flew the first aircraft in 1903. With the continuous development of technology, aircraft technology has also been improved. The three well-known flight mechanisms of aircraft are fixed-wing [1], rotary-wing [2], and flapping-wing [3] respectively. All three mechanisms change the pressure difference between the two sides of the airfoil to obtain lift. Fixed-wing generates lift by passing airflow through the airfoil with a fixed shape and angle of attack [4]. Rotary-wing generates lift and thrust through the interaction of airflow produced by the rotation of two propeller blades [5-6]. Flapping-wing generates lift by adjusting the vibration frequency and angle of flapping wings to form a series of

[1] Corresponding autho: Shengyou DUAN, Leicester International Institute, Dalian University of Technology, Panjin, Liaoning Province, 124221, China; e-mail: 1647005177@mail.dlut.edu.cn

vortices and eddies, thus creating a low-pressure area below the wings and obtaining upward lift [7-9].

The flight ability of birds is a biological miracle as they successfully combine fixed-wing and flapping-wing flight mechanisms. In the fixed-wing flight mode, birds unfold their wings, adjust their shape and angle to create lift, and use aerodynamic principles to hover or glide in the air, reducing energy consumption. In the flapping-wing flight mode, birds quickly flap their wings, consuming a large amount of energy to obtain lift and thrust [10]. This composite flight mode allows birds to maintain stability at a low speed and make rapid turns at a high speed. Although significant progress has been made in the aerodynamic research of airfoils, many related scientific issues remain unresolved. For example, the initial position of flow separation is an important factor affecting the aerodynamic performance of an airfoil. In the early stages of airfoil aerodynamic research, the Wright brothers tested more than 200 airfoil designs that mimic the shape of bird wings in their wind tunnel. Pearcey [11] discovered the existence of shock-free airfoils under supercritical pressure and invented peak airfoils. Zhang et al. [12] carried out research on the multi-objective optimization design of hypersonic vehicle airfoil in a wide velocity domain and obtained the Pareto frontier of optimized airfoil lift-drag ratio in different velocity domains. Yang et al. [13] promoted the development of the Chinese Dove by studying flexible wing design, flapping mechanism design, and on-board avionics development.

Compared with the study of single-bird flight, the study of bird formation flight is of more important significance. It can provide a reference for the aerodynamic principle of aircraft formation flight and reveal the strategies of birds adapting to the environment in the evolutionary process. There are two main forms of formation flight in birds: one is the “V” shape, in which the leading bird is in front. Other birds are divided into two rows to follow, forming a V-shaped formation [14]; The other is a “straight line” shape, in which all birds line up in a straight line with the leading bird in front and other birds following, forming a formation similar to a straight line to make turns smoother. In 1994, Cutts and Speakman [15] conducted multidimensional imaging on 54 pink-footed geese, calculated the average wingtip spacing and depth of geese flying in “V” formation and found that “V” formation could achieve 14% energy-saving. Heppner [16] suggested that the fixed position of the eyes in the heads of line-flying birds might make a staggered formation advantageous for keeping the image of an adjacent bird on the visual axis of a given bird’s eyes. Compared with the “V” shape formation, the “straight line” shape formation is easier to maintain and coordinate the flight direction, giving them a broader perspective. As a special form of the “straight line” shape formation, the front and rear arrangement is easier to analyze and understand, which has high research value. Therefore, this study mainly focuses on the aerodynamic characteristics of “straight line” shape bird formation flight. In recent years, there has been growing interest in using UAVs for various applications, including surveillance, search and rescue, and environmental monitoring. By studying the aerodynamic characteristics of bird formation flight, better strategies can be potentially developed for UAV formation flight, leading to more efficient and effective use of these devices in practical applications.

Since the 21st century, computer science and numerical simulation methods have achieved rapid development. Compared with traditional experiments, numerical simulation of airfoil aerodynamic characteristics takes the advantage of simulating complex flow phenomena, obtaining abundant aerodynamic parameters, and conducting parametric research [17]. It is an indispensable and important method in the research of airfoil aerodynamic characteristics [18-19]. Commonly used numerical simulation

methods for airfoil aerodynamics include methods for solving the Euler equation [20-21], solving the Navier-Stokes equation [22-23], mixed Euler Lagrange method [24], and methods based on boundary elements [25-26]. Among them, the Navier-Stokes equation can be used to precisely represent both the macroscopic and microscopic motion properties of fluids. Numerical methods for solving the Navier-Stokes equation are relatively mature and have been widely applied in scientific research and engineering fields. For example, Lan and Sun [27] studied the aerodynamic interactions of two airfoils in tandem configuration moving parallelly forward and down at a large angle of attack after an initial acceleration from rest, using the method of solving the Navier-Stokes equations in moving overset grids, which simulated the formation flight of birds. Charkraborty and Roy [28] found the solution of the Navier-Stokes equations of motion for the modeled double-gyre wake, identified the mechanistic signal transmission through wakes and elucidated the transport of the signals in a modeled dipolar double-gyre wake in formation flight. Although scholars have carried out a lot of research on the formation flight of birds, there is still a lack of a description of the flow phenomenon and explanation of aerodynamic principles. This study conducts in-depth numerical simulation and mechanism research to solve the above problems. In this study, two-dimensional numerical models of upstream and downstream wings are first established to visualize the aerodynamic characteristics caused by the interaction between the front and rear airfoils. Then, based on the dynamic results of unsteady flow phenomena, the correlation between vortices and wing forces is further analyzed. Finally, an explanation of the principle of bird formation flight is provided.

The remainder of this paper is organized as follows. In Section 2, the 2D numerical simulation method is introduced, followed by the descriptions of computational domain and boundary conditions. In Section 3, the aerodynamics data extraction and airfoil force characteristics are analyzed in detail. The aerodynamic characteristics and explanation of bird formation flight are identified. Conclusions are drawn in Section 4.

2. Methodology

2.1. Governing Equations in this Study

In this study, the Navier-Stokes equations of two-dimensional incompressible unsteady flow are solved to analyze the dynamic characteristics of the linear formation flight of birds. Wherein, the governing equations of two-dimensional incompressible unsteady flow are as follows:

$$\frac{\partial u}{\partial x}+\frac{\partial v}{\partial y}=0 \tag{1}$$

$$\frac{\partial u}{\partial t}+\frac{\partial uu}{\partial x}+\frac{\partial uv}{\partial y}=-\frac{1}{\rho}\frac{\partial P}{\partial x}+\frac{\mu}{\rho}\left(\frac{\partial^2 u}{\partial x^2}+\frac{\partial^2 u}{\partial y^2}\right) \tag{2}$$

$$\frac{\partial v}{\partial t}+\frac{\partial uv}{\partial x}+\frac{\partial vv}{\partial y}=-\frac{1}{\rho}\frac{\partial P}{\partial y}+\frac{\mu}{\rho}(\frac{\partial^2 v}{\partial x^2}+\frac{\partial^2 v}{\partial y^2}) \tag{3}$$

where u and v are the velocity components in x and y directions.

In this study, the chord length of the airfoil is selected as the characteristic length. The velocity of the inlet flow is selected as the characteristic velocity. The nondimensionalization of Equations (1-3) is carried out and dimensionless parameters are defined as follows:

$$t_0=\frac{l}{u_\infty} \tag{4}$$

$$P_\infty=\rho u_\infty^2 \tag{5}$$

$$\bar{t}=\frac{t}{\frac{l}{u_\infty}} \tag{6}$$

$$\bar{P}=\frac{P}{\rho u_\infty^2} \tag{7}$$

$$\mathrm{Re}=\frac{u_\infty l\rho}{\mu} \tag{8}$$

where Re is the Reynolds number.

The dimensionless two-dimensional incompressible unsteady Navier-Stokes equation can be written as

$$\frac{\partial \bar{u}}{\partial \bar{x}}+\frac{\partial \bar{v}}{\partial \bar{y}}=0 \tag{9}$$

$$\frac{\partial \bar{u}}{\partial \bar{t}}+\frac{\partial \overline{uu}}{\partial \bar{x}}+\frac{\partial \overline{uv}}{\partial \bar{y}}=-\frac{1}{\rho}\frac{\partial \bar{P}}{\partial \bar{x}}+\frac{1}{\mathrm{Re}}(\frac{\partial^2 \bar{u}}{\partial \bar{x}^2}+\frac{\partial^2 \bar{u}}{\partial \bar{y}^2}) \tag{10}$$

$$\frac{\partial \bar{v}}{\partial \bar{t}}+\frac{\partial \overline{uv}}{\partial \bar{x}}+\frac{\partial \overline{vv}}{\partial \bar{y}}=-\frac{1}{\rho}\frac{\partial \bar{P}}{\partial \bar{y}}+\frac{1}{\mathrm{Re}}(\frac{\partial^2 \bar{v}}{\partial \bar{x}^2}+\frac{\partial^2 \bar{v}}{\partial \bar{y}^2}) \tag{11}$$

2.2. Computational Domain and Boundary Conditions

In this study, two typical NACA0012 airfoils [29-30] are used, which are placed horizontally front and rear in the computational domain. The pitch angle is 4 degrees and the Reynolds number is 10,000 which represents the typical flight status of large birds, as shown in Figure 1.

The geometric shape of the computational domain is rectangular. Based on the characteristic scale of the airfoil chord length, the airfoil length is calculated as 1. The upstream boundary is 2 times the airfoil chord length from the front airfoil head and the airfoil spacing is 1 airfoil chord length. The downstream boundary is 5 times the airfoil chord length from the rear airfoil tail. The boundary distance between the upper and lower calculation domains is 2 times the chord length of the airfoil.

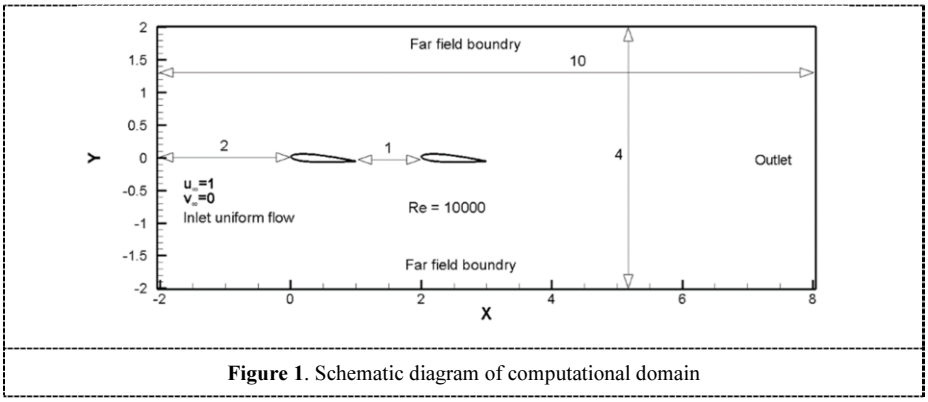

Figure 1. Schematic diagram of computational domain

Uniform airflow passes through the calculation domain from left to right, and the boundary conditions are:

1) The left boundary of the computational domain: inlet boundary conditions, uniform flow, $u\big|_{Inlet} = u_\infty = 1 \quad v\big|_{Inlet} = v_\infty = 0$

2) The right boundary of the computational domain: outlet boundary conditions, fully developed outflow, $\left.\frac{\partial u}{\partial x}\right|_{Outlet} = 0 \quad \frac{\partial v}{\partial x}_{Outlet} = 0$

3) Upper and lower boundaries of the computational domain: far-field boundary conditions, $\left.\frac{\partial u}{\partial y}\right|_{Lower/Upper} = 0 \quad \frac{\partial v}{\partial y}_{Lower/Upper} = 0$

4) Airfoil surface: wall condition, no-slip condition, $u\big|_{Wall} = 0 \quad v\big|_{Wallt} = 0$

As shown in Figure 2, a household complete orthogonal meshing code is used to generate meshes with 700 mesh points in the length direction and 514 mesh points in the width direction. 131 mesh points are arranged on the surface of the NACA0012 airfoil. The mesh has been densified near the wall and in areas where vortex generation is active. The household incompressible unsteady Navier-Stokes solver based on the finite volume method was used in this study with second-order spatial and temporal discretization schemes. The unsteady dimensionless time advance step is $\Delta t = 0.0002$.

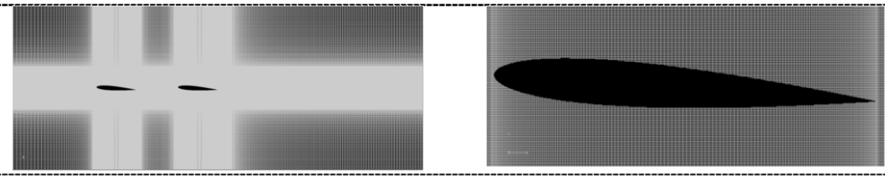

Figure 2. Generation of simulation mesh. (a) Global mesh; (b) Local mesh (near airfoil).

3. Results and Discussions

3.1. Aerodynamic Characteristics Analysis

3.1.1. Airflow Velocity Around the Front and Rear Airfoils

Figure 3 shows the magnitude and direction of airflow velocity near the front and rear airfoil. The main characteristics are as follows:

1) As shown in Figure 3 (a), influenced by the boundary conditions and wall conditions, the dimensionless airflow velocity direction in the computational domain is horizontal from the inlet to the outlet with a magnitude of 1.0. The airflow velocity magnitude decreases with increasing proximity to the airfoil surface. The velocity magnitude reaches the minimum value of 0 on the front and rear airfoil surface. The airflow has a maximum velocity of 1.5, which appears on the upper surface of the front airfoil, the upper and lower surfaces of the rear airfoil, and their downstream regions.

2) As shown in Figures 3 (b) and 3 (c), the dimensionless horizontal distance between the air separation point on the front airfoil and its leading edge is 0.425. The horizontal distance between the air separation point on the rear airfoil and its leading edge is 0.465. The distance between the air separation point on the rear airfoil and its leading edge is about 1.094 times that between the air separation point on the front airfoil and its leading edge. Figures 3 (d) and 3 (e) depict the separation in more detail. Because of the existence of the negative airflow with a velocity of about 0 - 0.3 in the area of air separation, the airfoil can obtain less lift force. Therefore, the closer the separation point is to the trailing edge, the smaller the area of air separation is and the greater the lift force acting on the airfoil is.

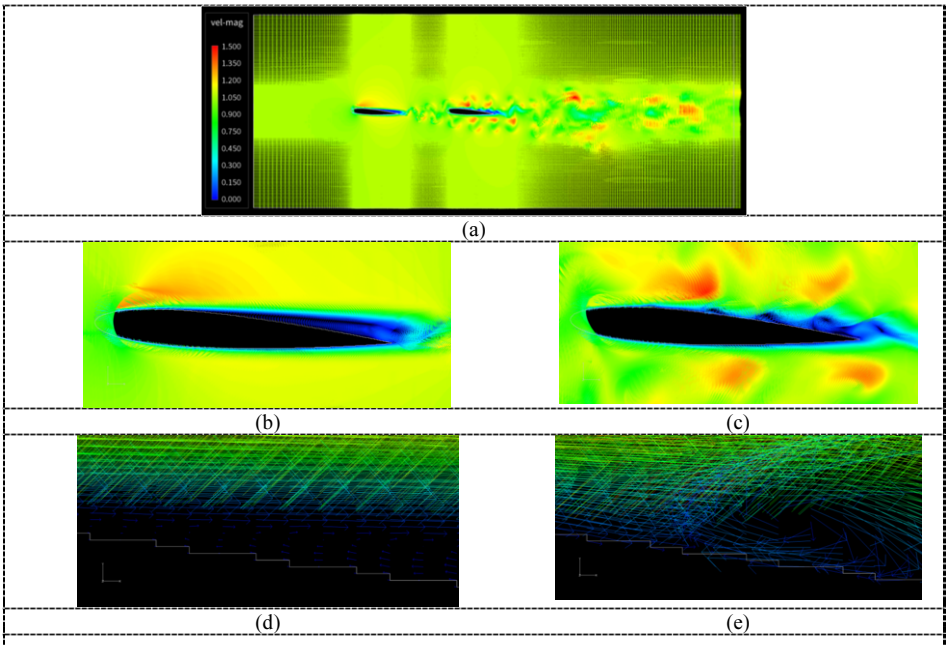

Figure 3. Vector diagram of airflow velocity around front and rear airfoils. (a) Computational domain; (b) Front airfoil; (c) Rear airfoil; (d) Separation on front airfoil; (e) Separation on the rear airfoil

From the perspective of airflow velocity, the rear airfoil can get more lift than the front airfoil does in formation flight because under the influence of wake interference, the separation area of the rear airfoil is smaller and it can get more lift under the condition of less negative airflow.

3.1.2. Pressure Around the Front and Rear Airfoils

Figure 4 shows the pressure gradient of the airflow near the front and rear airfoil. The main characteristics are as follows:

1) For both of the airfoils, the minimum dimensionless pressure reaches -0.522, which occurs above the leading edge. The maximum pressure reaches 0.417, which occurs below the leading edge of the airfoil. The low and high-pressure areas are formed around the highest and lowest pressure respectively. The pressure range of the low-pressure region on the upper surface is between -0.522 and -0.120. The pressure range of the high-pressure region on the lower surface is between 0.072 and 0.417. It can be observed that the area of the low-pressure region on the upper surface is significantly higher than that of the high-pressure region on the lower surface. Therefore, the lift force of the airfoil is mainly generated by the upper surface. As time goes by, high and low pressure will occur on the upper and lower surfaces at the same time, but the area of the low-pressure area on the upper surface is significantly higher than that of the high-pressure area on the lower surface, which has not been changed.

2) Vortices formed and detached at the trailing edge of the front airfoil are generated by airflow with pressure from -0.240 to -0.146. Under the interference of the vortices detached from the front airfoil, the vortices generated on the rear airfoil are close to the leading edge. The vortices existing on the upper and lower surface of the rear airfoil are generated by airflow with pressure from -0.428 to -0.053 and -0.334 to -0.146. The same vortices only occur near the trailing edge of the front airfoil. Compared with the pressure contours on the front airfoil, the denser pressure contours on the upper and lower surfaces of the rear airfoil affected by vortices from wake interference indicate a greater pressure difference between the upper and lower ends and the higher lift on it.

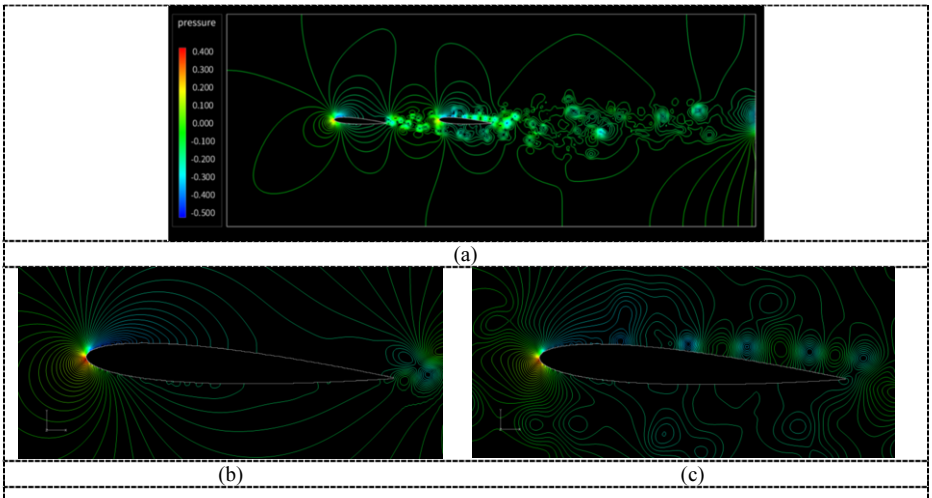

Figure 4. Pressure contour around front and rear airfoils. (a) Computational domain; (b) Front airfoil; (c) Rear airfoil.

From the perspective of pressure, under the influence of wake interference, there are more vortices on the rear airfoil surface. The vortices generated by the rear airfoil surface increase the rate of pressure change in space. The resulting denser pressure contour near the rear airfoil indicates that the upper and lower surfaces produce a larger pressure difference, making the rear wing obtain more lift than the front airfoil does.

3.2. Mechanics Characteristics of Airfoils

3.2.1. Analysis of Time-domain Images

The three typical mechanical characteristics of bird formation flight are lift, pressure and viscous drag. Lift is the upward force perpendicular to the direction of motion that the airfoil receives when it moves. The drag caused by the difference in pressure applied to the front and back of the airfoil is called pressure drag. Viscous drag is the resistance of a fluid to flow as a type of friction in fluids. The relationships between the three dimensionless coefficients: lift, pressure drag, viscous drag coefficient and time are shown in Figure 5. It is found that after 15 seconds, the airflow velocity and pressure gradient around the airfoils reach a stable period and no significant changes occur. Therefore, the lift coefficient, pressure drag coefficient and viscous drag coefficient of the two airfoils after 15 seconds are selected as analysis objects, The results of the analysis are as follows:

1) As shown in Figure 5 (a), the average lift coefficient of the rear airfoil is 0.1053, which is 13.71% higher than that of the front airfoil at 0.0926. The amplitude of the lift coefficient of the rear airfoil is 0.0847, which is about 2.98 times greater than that of the front airfoil of 0.0284.

2) As shown in Figure 5 (b), the average pressure drag coefficient of the rear airfoil is 0.0123, which is 19.08% lower than that of the front airfoil of 0.0152. The amplitude of the lift coefficient of the rear airfoil is 0.0026, which is about 1.73 times greater than that of the front airfoil of 0.0015.

3) As shown in Figure 5 (c), the average viscous drag coefficient of the rear airfoil is 0.0093, which is 14.68% lower than that of the front airfoil of 0.0109. The amplitude of the viscous drag coefficient of the rear airfoil is 0.0004, which is about 1.33 times greater than that of the front airfoil of 0.0003.

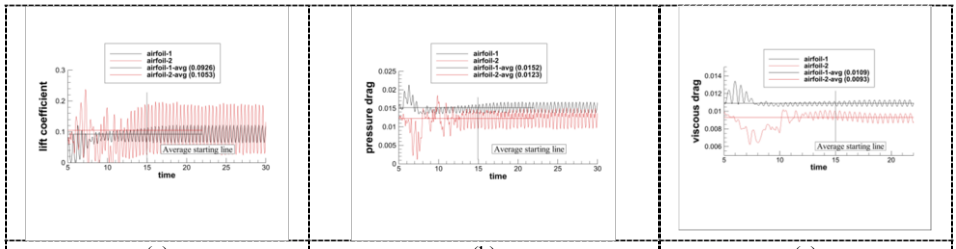

(a) (b) (c)

Figure 5. Relationship between lift, pressure drag, viscous drag coefficient and time. (a) Lift coefficient; (b) Pressure drag coefficient; (c) Viscous drag coefficient.

To sum up, in the "straight line" shape formation flight, the rear airfoil has a higher lift coefficient, lower pressure drag and viscous drag coefficient than the front airfoil. Compared with the leading bird, the following bird can gain higher lift and less energy consumption, thus improving its flight efficiency.

3.2.2. Analysis of Frequency Domain Images

The frequency domain analysis results obtained by using the Fourier Transform are shown in Figure 6.

1) The component with zero frequency is the direct current component and its amplitude represents the average magnitude of the corresponding coefficients, which is equal to the average value of the coefficients in Figure 5. The fundamental frequency of the signals is 2.21.

2) For the frequency domain image with three coefficients of the front airfoil, only an obvious fundamental wave can be observed, but no obvious harmonic wave can be observed. The fundamental amplitude of the front airfoil lift coefficient is 0.0240. The fundamental amplitude of the viscous drag coefficient is 0.00119. The fundamental amplitude of the lift coefficient is 0.000309.

3) In the frequency domain image with three coefficients of the rear airfoil, both fundamental and low-order harmonics can be observed. The fundamental amplitude of the rear airfoil lift coefficient is 0.0674. The first-order harmonic amplitude is 0.00298. The fundamental amplitude of the rear airfoil pressure drag coefficient is 0.00166. The first and second-order harmonic amplitudes are 0.000659 and 0.000173 respectively. The fundamental amplitude of the rear airfoil viscous drag coefficient is 0.0005. The first-order harmonic amplitude is 0.000231.

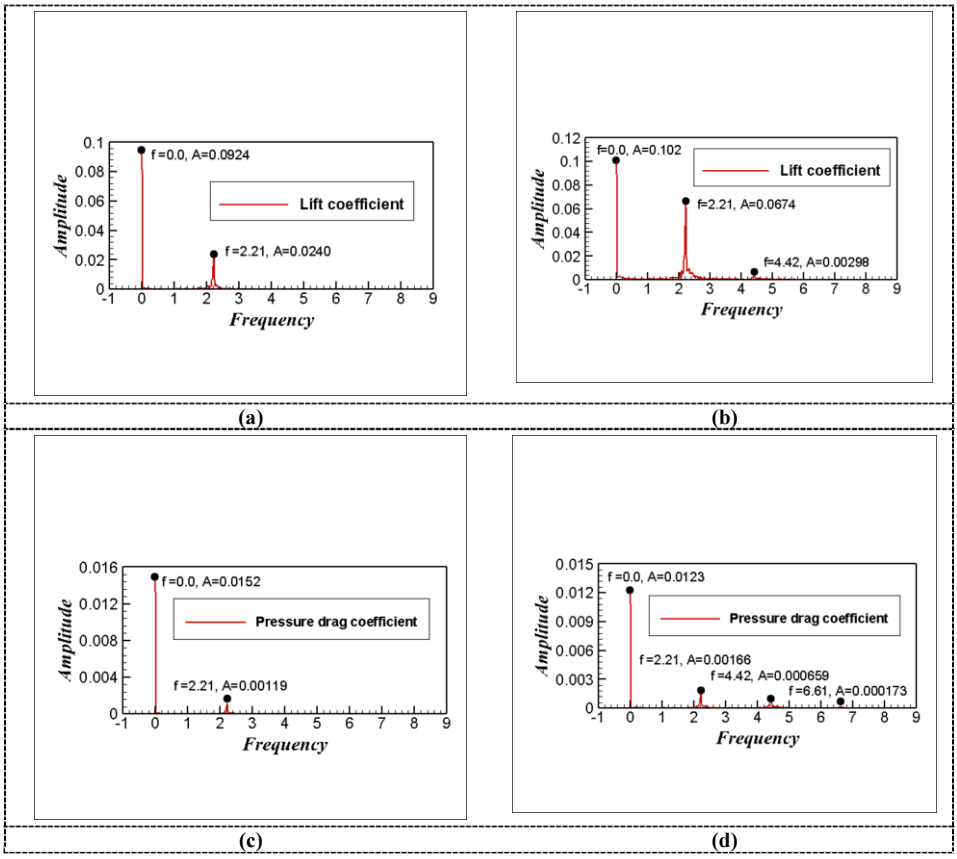

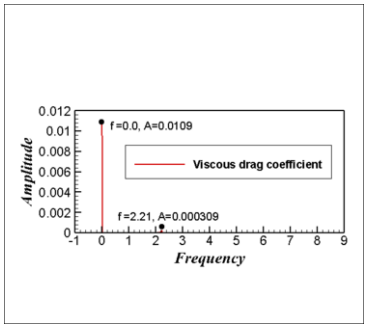

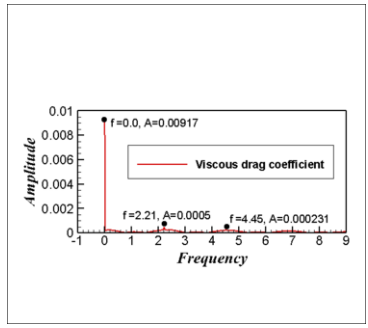

(e) (f)

Figure 6. Relationship between coefficient amplitude and frequency. (a) Front airfoil lift; (b) Rear airfoil lift; (c) Front airfoil pressure drag; (d) Rear airfoil pressure drag; (e) Front airfoil viscous drag; (f) Rear airfoil viscous drag.

In the frequency domain images of the rear airfoil, the amplitude of the fundamental wave and the same order harmonics in the frequency domain image is greater than that of the front airfoil. This is the reason why the three coefficients of the rear airfoil in the time domain image are greater than that of the front airfoil. The larger the amplitude of the harmonic component is, the greater the proportion of the harmonic in the signal is, the greater the influence on the characteristics of the signal is. Therefore, there are more factors affecting the lift, pressure drags, and viscous drag of the rear airfoil than that of the front airfoil.

3.3. Observation and Characteristics of Flow Phenomena

3.3.1. Dynamic Simulation of Airflow

The visualization of flow characteristics using tracer particles is shown in Figure 7. As shown, the upwash draws surrounding air above the surface of the airfoil. The airflow on the surface of the airfoil becomes smoother, reducing the friction between the air and the surface, and thus reducing the viscous drag. The airflow passing through the front airfoil forms vortices at the trailing edge. The intensity of the upwash in front of the leading edge of the rear airfoil is significantly greater than that of the front edge of the front airfoil. As a result, the viscous drag on the rear airfoil is lower than that on the front airfoil.

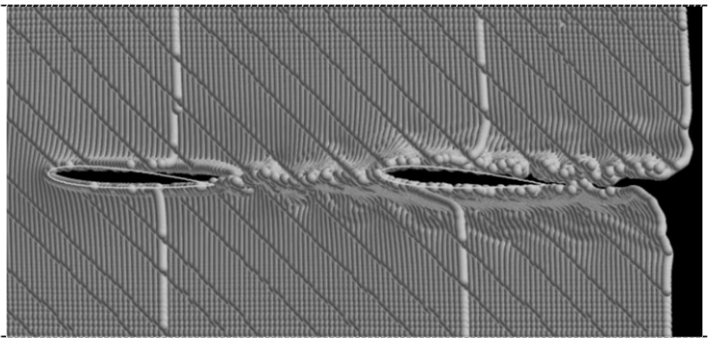

Figure 7. Dynamic simulation of flow around front and rear airfoils

3.3.2. Dynamic Simulation of Vortices and Vorticity Distribution.

The vortex state around the front and rear airfoils is dynamically simulated, as shown in Figure 8. By observing the flow phenomenon, it is found that:

1) For the front airfoil, the airflow on the upper and lower surfaces of the airfoil is disturbed by the front airfoil vortices. In the airflow around the airfoil, a vortex with negative vorticity forms on the upper surface of the airfoil, while a vortex with positive vorticity forms on the lower surface of the airfoil. These two vortices with angular velocity in opposite directions periodically shed near the trailing edge of the front airfoil. The maximum absolute vorticity is 3.00 at the center of the vortices and the magnitude of the value decreases as the distance from the center of the vortex increases. At the outermost layer, its value is 0. This shedding causes periodic changes in the pressure difference between the upper and lower surfaces of the airfoil, so a pulsating lift force is generated on the front airfoil.

2) For the rear airfoil, the composition of the lift is more complex. In addition to the factor that the airflow itself accumulates in the leading edge of the airfoil and falls off in the form of vorticity at the trailing edge, the wake of the front airfoil will also interfere and cause partial influence. Compared with the front airfoil, the position where the vortex sheds from the upper surface of the rear airfoil is closer to the leading edge. The distance between the position where the complete vortex appears and the leading edge is about 0.4 times the chord length, that is 0.4. The maximum and minimum vorticity detached from the upper and lower surfaces of the rear airfoil does not change with the maximum value remaining 3.00 and -3.00 and the minimum value remaining 0. Under the disturbance of the wake, there are about four vortices on the upper surface at the same time, which means four times the number of vortices on the upper surface of the front airfoil. Due to the relatively close distance in formation flight in the model, which is only one chord length, the counter-clockwise vortices generated by the front airfoil after a series of merging and canceling are more distributed on the upper surface of the rear airfoil, while the clockwise vortices are more distributed on the lower surface of the rear airfoil. As a result, under the impact of wake interference, the effect of vortex shedding on the rear airfoil is more obvious than that on the front airfoil. The lift on the rear airfoil is greater than the lift on the front airfoil.

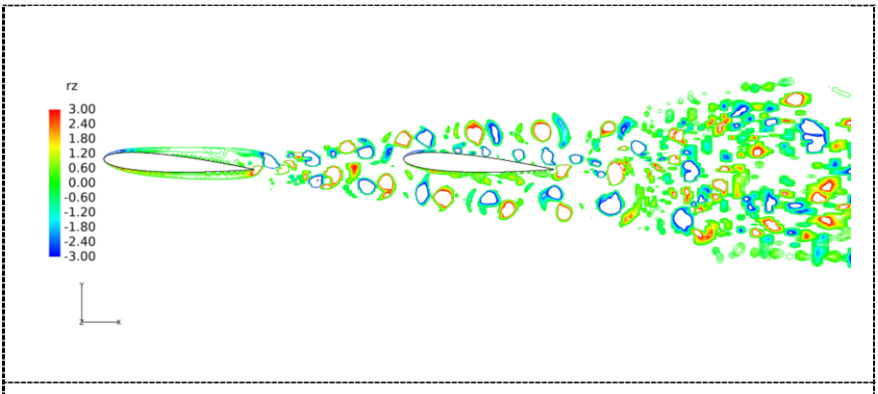

Figure 8. Dynamic simulation of vorticity distribution around front and rear airfoils

By observing and summarizing the aerodynamic interactions of the wings arranged in a “straight line” shape, it can be concluded that the formation flying phenomena of

birds is an application of wake interference. The lead bird changes the distribution of airflow around the wings, which affects the aerodynamic performance of the wings of other birds. This is illustrated in terms of velocities, pressures, and vortices in this study.

4. Conclusion

In this study, from the perspectives of aerodynamic characteristics analysis, mechanical characteristics of airfoils, and characteristics of flow phenomena, 2D numerical aerodynamics simulation numerical aerodynamic simulation used to explain the formation flight phenomenon of birds is analyzed and discussed. The results of the analysis are as follows:

1) By analyzing airflow velocity, the position of the air separation point is obtained and compared. The distance between the air separation point on the rear airfoil and its leading edge is about 1.094 times that between the air separation point on the front airfoil and its leading edge. By analyzing the pressure gradient, the pressure distribution and contrast around the airfoils are clarified in combination with the vortices formed by airflow. For both of the airfoils, the pressure range of the low-pressure region on the upper surface is between -0.522 and -0.120. The pressure range of the high-pressure region on the lower surface is between 0.072 and 0.417. The vortices existing on the upper and lower surface of the rear airfoil are generated by airflow with pressure from -0.428 to -0.053 and -0.334 to -0.146, which only occurs near the trailing edge of the front airfoil.

2) Three dimensionless physical quantities of bird formation flight: lift, pressure drag, and viscous drag coefficient are compared to demonstrate the advantages of formation flight. The average lift coefficient of the rear airfoil is 13.71% higher than that of the front airfoil. The average pressure drag coefficient of the rear airfoil is 19.08% lower than that of the front airfoil. The average viscous drag coefficient of the rear airfoil is 14.68% lower than that of the front airfoil.

3) The influence mode of wake interference on vortex shedding is discussed through the analysis of the vorticity diagram. The maximum and minimum vorticity detached from the upper and lower surfaces of the rear airfoil is the same for both airfoils with the maximum value remaining at 3.00 and -3.00 and the minimum value of 0. Under the disturbance of the wake, there are about four times as many vortices on the upper surface of the rear airfoil as there are on the upper surface of the front airfoil.

These analysis results confirm that the formation flight of birds is not an accident, but an energy-saving way of flight based on the principles of aerodynamics, and reveal the strategies of the evolution of birds to gradually adapt and exploit their environment. The potential is demonstrated to use nature-inspired principles to improve the efficiency and sustainability of UAV formation flight.

References

[1] Zhang, X. C., Wan, Z. Q., Zhang, Y.Y., et al. (2016) Conceptual design of rotary wing and fixed wing compound VTOL aircraft. Acta Aeronautica et Astronautica Sinica, 37: 179-192.

[2] Li, J. Y., Lan, Y.B., Shi, Y. Y. (2018) Research progress on airflow characteristics and field pesticide application system of rotary-wing UAV. Transactions of the Chinese Society of Agricultural Engineering, 34: 104-118.

[3] Xu, W. J., Yao, K., Song A. L., et al. (2020) Survey of research on small and micro bionic flapping wing

aircraft. Cyber Security and Data Governance, 39 (10): 7-10.
[4] Chen, W. D., Ning, L., Liu, M.Q., et al. (2015) Simulation of small fixed-wing aircraft flight dynamics. Flight Dynamics, 33: 301-305.
[5] Zuo, C.L., Ma, J., Yue, T. R., et al. (2020) Displacement and deformation measurements of helicopter rotor blades based on binocular stereo vision. Journal of Experiments in Fluid Mechanics, 34: 87-95.
[6] Wang, P., Li, Y., Cui, G., et al. (2021) Rotor unmanned aerial vehicle, a new design, new application and new development. AI-View, 23: 78-91.
[7] He, W., Liu, S. P., Huang, H. F., et al. (2022) System design and experiment of an independently driven bird-like flapping-wing robot. Control Theory and Applications, 39: 12-22.
[8] Xie, Z. M., Hu, C., Wang, X. Z. (2021) Simulation and Comparative Analysis of High Lift Mechanism during Flapping-wing Flight. Journal of Xi'an Aeronautical Institute, 39: 26-32.
[9] Song, B. F., Lang, X. Y., Xue, D., et al. (2022) A review of the research status and progress on the aerodynamic mechanism of bird wings. Scientia Sinica (Technologica), 52: 893-910.
[10] Zhang, Z. J., Chen, M., Yang, H, J., et al. (2021) Analysis of Aerodynamic Characteristics of Bionic Flapping Wing Aircraft Based on XFlow. Journal of Northeastern University(Natural Science), 42: 821-828.
[11] Pearcey, H. H. (1962) The aerodynamic design of section shapes for swept wings. In: Theodore, V.K. (Eds.), Advances in Aeronautical Sciences. Elsevier, Amsterdam. pp. 277-322.
[12] Zhang, Y., Han, Z. H., Liu, F., et al. (2019) Multi-Objective Aerodynamic Shape Optimization of Wide-Mach-Number-Range Airfoil. Physics of Gases, 4: 26-40.
[13] Yang, W., Wang. L., Song, B. (2017) "Dove": A biomimetic flapping-wing micro air vehicle. International Journal of Micro Air Vehicles, 10: 70-84.
[14] Cutts, C., Speakman, J. (1994) Energy savings in formation flight of pink-footed geese. Journal of Experimental Biology, 189: 251-261.
[15] Qu, Q. L., Wang, J. J. (2016) Human flight inspired by the aerodynamics of bird flight. Physics, 45: 640-644.
[16] Iztok, L.B., Frank, H. (2012) Organized flight in birds. Animal Behaviour, 78: 777-789.
[17] Wang, P., Jin, X. (2019) Study on artificial neural network modeling and wind tunnel test for the FADS system applied to the vehicle with sharp-nosed fore-bodies. Journal of Experiments in Fluid Mechanics, 33: 58-64.
[18] Fu, Q., Zhang, X., Zhao, M., et al. (2022) Research progress on the wind tunnel experiment of a bionic flapping-wing aerial vehicle. Chinese Journal of Engineering Science, 44: 767-779.
[19] Gao Y. B., Geng L. L., Wang Z., et al. (2022) A review of numerical models development for gas-liquid two-phase flow based on Eulerian–Eulerian method. Mechanics in Engineering, 44: 1021-1036.
[20] Meng, W. A., Mutalif A., Yan R. B. (2012) Numerical research on the flow field of T-tube by mix-multiphase flow model and Euler-multiphase flow model. Machinery Design & Manufacture, 252: 27-29.
[21] Guo, M. L., Wang, F. J., Tan J. J., et al. (2019) Meshless method coupled with different Reynolds average turbulence model for solving Navier-Stokes equation. Journal of Nanjing University of Science and Technology, 43: 548-555.
[22] Zhao, Q. J., Zhao, G. Q., Wang B., et al. (2018) Robust Navier-Stokes method for predicting unsteady flowfield and aerodynamic characteristics of helicopter rotor. Chinese Journal of Aeronautics, 31: 214-224.
[23] Chen, Y. F., Zheng, Y. Y. (2020) A discontinuous Galerkin FEM for 2D Navier-Stokes equations of incompressible viscous fluids. Applied Mathematics and Mechanics, 41: 844-852.
[24] Liu, X. J., Shi, L., Xu, X. C. (2007) Activities of dense particle-gas two-phase flow modeling in Eulerian-Lagrangian approach. Chinese Journal of Computational Mechanics, 41: 166-172.
[25] Deng, Q., Guo, M.W., Li, C. G., et al. (2010) Vector sum method for slope stability analysis based on boundary element method. Rock and Soil Mechanics, 31: 1971-1976.
[26] Liu, Y., Li, J., Hu, Q. Y., et al. (2020) Some advances in boundary element methods. Mathematica Numerica Sinica, 42: 310-348.
[27] Lan, S. L., Sun, M. (2001) Aerodynamic interactions of two airfoils in unsteady motion. Acta Mechanica, 150: 39-51.
[28] Chakraborty, P., Roy, A. (2022) Wake aerodynamics of flapping systems in formation flight. Physics of Fluids, 34: 47113.
[29] Rodríguez, I., Lehmkuhl, O., Borrell, R., et al. (2013) Direct numerical simulation of a NACA0012 in full stall. International Journal of Heat and Fluid Flow, 43: 194-203.
[30] Chang, J. L., Zhang, Q. G., He, L. J., et al (2022) Shedding vortex characteristics analysis of NACA 0012 airfoil at low Reynolds numbers. Energy Reports, 8: 156-174.